

Chitin Nanofibrils from Fungi for Hierarchical Gel Polymer Electrolytes for Transient Zinc-Ion Batteries with Stable Zn Electrodeposition

Diego Ruiz, Veronica F. Michel, Markus Niederberger,* and Erlantz Lizundia*

Rechargeable batteries play an integral role toward carbon neutrality. Environmentally sustainable batteries should consider the trade-offs between material renewability, processability, thermo-mechanical and electrochemical performance, as well as transiency. To address this dilemma, we follow circular economy principles to fabricate fungal chitin nanofibril (ChNF) gel polymer electrolytes (GPEs) for zinc-ion batteries. These biocolloids are physically entangled into hierarchical hydrogels with specific surface areas of $49.5 \text{ m}^2 \cdot \text{g}^{-1}$. Ionic conductivities of $54.1 \text{ mS} \cdot \text{cm}^{-1}$ and a Zn^{2+} transference number of 0.468 are reached, outperforming conventional non-renewable/non-biodegradable glass microfibre separator–liquid electrolyte pairs. Enabled by its mechanically elastic properties and large water uptake, a stable Zn electrodeposition in symmetric Zn|Zn configuration with a lifespan above 600 h at $9.5 \text{ mA} \cdot \text{cm}^{-2}$ is obtained. At $100 \text{ mA} \cdot \text{g}^{-1}$, the discharge capacity of Zn/ α - MnO_2 full cells increases above 500 cycles when replacing glass microfibre separators with ChNF GPEs, while the rate performance remains comparable to glass microfibre separators. To make the battery completely transient, the metallic current collectors are replaced by biodegradable polyester/carbon black composites undergoing degradation in water at $70 \text{ }^\circ\text{C}$. This work demonstrates the applicability of bio-based materials to fabricate green and electrochemically competitive batteries with potential applications in sustainable portable electronics, or biomedicine.

material scarcity is an urgent endeavor to reach the climate-neutral goals set by the Paris Agreement. Although rechargeable batteries are a key enabler technology for decarbonization,^[1] current lithium-ion battery (LIB) designs do not adhere to circular economy strategies aimed to use abundant, non-toxic, cheap, and renewable/bio-degradable materials to construct long lifespan (re-use strategy) batteries.^[2] Multivalent ion-based batteries bearing metal anodes such as Mg, Al, and Zn are particularly attractive for sustainable rechargeable batteries because they combine earth-abundant materials with relatively large energy densities.^[3] Among those, the Zn-ion chemistry is attractive due to its ability to operate with near-neutral aqueous electrolytes,^[4] making batteries cheaper and greener. Additionally, water-based electrolytes enable larger ionic conductivities over organic-based electrolytes, facilitating the substitution of conventional separator–liquid electrolyte pairs by gel-like electrolytes with competitive ionic conductivities. Importantly, gel polymer electrolytes (GPEs) improve battery safety by avoiding uncontrolled electrolyte leakage,^[5] or

by conferring a flame-retardant character to the electrolyte.^[6] GPEs also limit the growth of high surface area metal deposits (dendrites) characteristic of organic liquid electrolytes that can result in battery short-circuit and ultimate explosion.^[7,8]


1. Introduction

The need for energy storage technologies counteracting current climate crisis, environmental pollution, and critical raw

D. Ruiz, V. F. Michel, M. Niederberger
Laboratory for Multifunctional Materials, Department of Materials
ETH Zurich
Vladimir-Prelog-Weg 5, Zurich 8093, Switzerland
E-mail: markus.niederberger@mat.ethz.ch

E. Lizundia
Life Cycle Thinking Group, Department of Graphic Design and
Engineering Projects, Faculty of Engineering in Bilbao
University of the Basque Country (UPV/EHU)
Bilbao 48013, Spain
E-mail: erlantz.liizundia@ehu.eus

E. Lizundia
BCMmaterials, Basque Center for Materials, Applications and Nanostructures
UPV/EHU Science Park
Leioa 48940, Spain

 The ORCID identification number(s) for the author(s) of this article can be found under <https://doi.org/10.1002/smll.202303394>

© 2023 The Authors. Small published by Wiley-VCH GmbH. This is an open access article under the terms of the Creative Commons Attribution-NonCommercial License, which permits use, distribution and reproduction in any medium, provided the original work is properly cited and is not used for commercial purposes.

DOI: 10.1002/smll.202303394

Recent life cycle assessment studies have observed reduced environmental footprints per 1 kWh of storage capacity of zinc-ion batteries (ZIBs) and Zn-air batteries over conventional LIBs, sodium-ion batteries, or lithium-sulfur batteries.^[9,10] The key factors for this superior environmental performance are the use of aqueous electrolytes over the toxic and flammable chemicals found in LIBs (lithium hexafluorophosphate, carbonate esters), the open-atmosphere assembly, the utilization of earth-abundant materials, and the less toxic character of the cathodes (MnO_2 is mostly used in ZIBs over the predominant cobalt-based chemistries in LIBs). However, attaining higher cyclability represents the most acute problem that needs to be solved to further reduce the complete life-cycle impacts and reach the carbon neutrality targets by 2050.^[11]

Accordingly, ZIBs are attractive to build green energy storage systems provided their service life can be prolonged. However, the quick dendritic failure of the Zn anode still needs to be upgraded,^[4] while the need for inorganic/non-biodegradable materials that build-up the separator and current collectors must be ideally avoided to ensure that batteries do not contaminate marine, river, or land environments if discarded inadequately.^[12] In this context, we focus our attention toward a recent work highlighting the potential of cellulosic bio-colloids to offer stable metal ion electrodeposition and enhance the operation life spans of batteries.^[8] Following circular bio-economy strategies aiming at exploiting biological resources and reintroducing end-of-life materials back into the economic circle,^[13] bio-waste can be valorized into high-performance valuable (nano)materials to replace conventional separators composed of non-renewable materials and solve both the electrochemical and environmental sustainability drawbacks of current ZIBs.^[14] Likewise, the inherent biodegradable character of bio-based materials can be exploited to fabricate secondary transient batteries, that is, batteries with the ability to be disintegrated, dissolved, or degraded into non-toxic products after a period of reliable operation. These batteries present the advantage of avoiding the water and land pollution issues associated with improperly disposed conventional batteries.

In contrast to the widely explored lignocellulosic biomass, the potential of fungal biomass remains to be investigated given the considerably less research undertaken.^[15] The inner cell wall in most fungal species presents a core of covalently attached branched β -glucan with chitin that assembles into microfibrils to provide structural stability to fungal cell walls.^[16] Importantly, chitin nanofibrils (ChNFs) are very easily extracted from fungi in comparison with the typical crustacean resources,^[17] opening the path toward high-performance green biocolloids. ChNF isolation solely produces 14.7–18.5 kg CO_2 -equiv·kg⁻¹,^[18] well below the 177.9–906.8 kg CO_2 -equiv·kg⁻¹ generated during conventional cellulose nanocrystal or chitin nanocrystal extraction. In addition, the nanoscale diameter and microscale length of these biocolloids result in high aspect ratios that enable their interaction, deformation, and ultimately entanglement into gels at low concentrations,^[19] making them highly attractive to obtain GPEs with large fractions of ionic species and high ionic conductivity values. ChNFs also enable rechargeable batteries with the potential to be degraded into non-toxic products after a period of stable operation.^[20,21] In spite of these merits, fungi-derived ChNFs

have never been explored either as gels or in the energy storage field.

Achieving green (renewable, biodegradable, and low carbon footprint) and electrochemically competitive batteries is a complex endeavor as the trade-offs between material renewability, biodegradability, processability, thermo-mechanical performance, rate capability, and operating lifespans should be carefully balanced.^[22–24] Here we tackle this challenge and design organic-waste (fungi) derived GPEs for ZIBs. First, a hydrogel composed of ChNF biocolloids extracted from mushroom presenting Zn^{2+} conductivities up to 54.1 mS·cm⁻¹ is obtained upon the combination of top-down and bottom-up processes. Chitin overcomes the sluggish ion migration issues resulting from the large crystalline fractions in conventional GPEs.^[5,6] Coupled with mechanically adaptable and elastic properties, homogeneous and reversible Zn electrodeposition onto Zn anode is obtained, enabling lifespans extending beyond 600 h and reaching current densities as high as 9.5 mA·cm⁻². Compared to conventional glass microfibre separators soaked into a liquid electrolyte short-circuit at 2.6 mA·cm⁻². When the ChNF electrolyte is assembled into a secondary Zn/ α - MnO_2 full cell, the long-term discharge capacity results improved in comparison with the cell assembled with the glass microfibre soaked in 2 M $\text{ZnSO}_4 \cdot \text{H}_2\text{O}$. To facilitate battery decomposition when discarded into the environment, the conventional current collectors based on non-biodegradable materials are replaced by electrically conducting nanocomposites prepared from biodegradable polymers and carbon black (CB). Battery transiency is proven by a proof-of-concept prototype that disintegrates in water at 70 °C to render non-toxic products. These results highlight the applicability of bio-waste to fabricate sustainable and electrochemically competitive energy storage devices that adhere to circular economy principles. Additionally, we envisage these novel electrolytes and current collectors to be applied for other battery chemistries aimed at environmental sustainability and long operation lifespans.

2. Experimental Section

2.1. Materials

Agaricus bisporus white mushrooms with a cap diameter of 27–42 mm were purchased from a local store in Zurich, Switzerland. Sodium hydroxide (NaOH) pellets (99%), glutaraldehyde (70% aqueous solution), potassium permanganate (KMnO_4 , $\geq 99\%$), manganese (II) acetate tetrahydrate ($\text{Mn}(\text{CH}_3\text{COOH})_2$, $\geq 99\%$), dichloromethane ($\geq 99.5\%$), ethyl lactate ($\geq 98\%$), and polycaprolactone (PCL) with an M_n of 80.000 g·mol⁻¹ were purchased from Sigma Aldrich. Poly(lactic acid) (PLA) with a number-average molecular weight (M_n) of 120.000 g·mol⁻¹ was kindly supplied by Corbion (Amsterdam, Netherlands), polybutylene adipate terephthalate (PBAT) was obtained from Natureplast (France) under the commercial name PBE 006, and they were all used as obtained. Super C65 conductive CB was purchased from Imerys ($>99.5\%$). 0.62 mm thick Zn foil (99.9%) was purchased from Alfa-Aesar. $\text{ZnSO}_4 \cdot 7\text{H}_2\text{O}$ (99.5%) was obtained from Acros Organics. Glass microfibre filters (Grade GF/D) were obtained from Whatman.

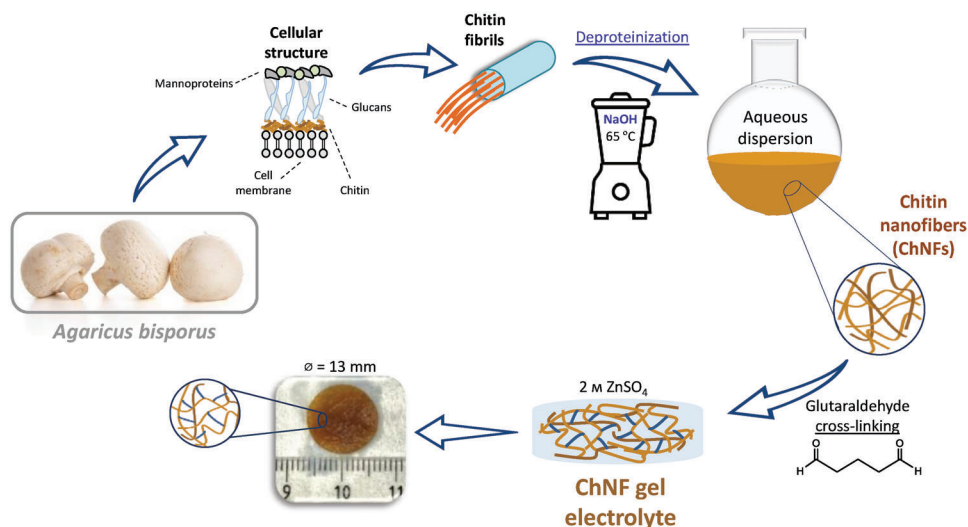


Figure 1. Schematic representation summarizing the synthesis of the chitin nanofibril GPEs. A top-down approach isolates colloidal chitin nanofibrils from mushroom (*Agaricus bisporus*). A never-dried aqueous dispersion is then used to prepare GPEs (diameters of ≈ 13 mm) according to a bottom-up process involving chemical cross-linking with glutaraldehyde and $2 \text{ M ZnSO}_4 \cdot \text{H}_2\text{O}$ infiltration.

2.2. ChNF Extraction

Colloidal ChNFs were isolated using a top-down approach using the whole fruiting body of the *Agaricus bisporus*, a commonly consumed mushroom worldwide. The process reported by Bismarck et al. has been followed,^[17] and it is summarized in **Figure 1**-top. First, the fruiting body of the as-received mushrooms was frozen at -19°C for 3 days to avoid undesired enzymatic degradation. For ChNF extraction, 1 kg of frozen mushrooms was thawed in 2 L distilled water for 5 min and further washed with water to remove impurities. The procedure was carried out three times with an initial 5 min blending in a kitchen blender (Stabmixer KOENIG). Next, a water treatment at 85°C for 30 min (1:30 w:v%) under continuous stirring removed the water-soluble components. After washing the material by centrifugation at 4000 rpm for 15 min, the residual solid was submitted to an additional treatment in 1 M NaOH at 65°C for 180 min (1:30 w:v%) under stirring to remove proteins, lipids, and alkaline-soluble polysaccharides. After washing, the remaining solids were neutralized and re-suspended in water to reach a concentration of 1% w/v and dispersed by final blending for another 1 min. The dispersion was stored at 4°C until use.

2.3. Fabrication of Biobased GPEs

As shown in **Figure 1**-bottom, GPEs were obtained using three different dispersions with concentrations ranging from 0.8 to 1.5 wt% of fungi-derived ChNF in water. Glutaraldehyde was added as a cross-linker to improve the mechanical stability of the hydrogels. Briefly, 52.5 mL of a ChNF aqueous dispersion was homogenized under continuous stirring for 30 min at 60°C . Then, different amounts of glutaraldehyde to reach 0.25, 1.0, and 2.0 wt% with respect to ChNF were added. The mixture was stirred for another 60 min at 60°C . Finally, the solution was poured into a 22.1 cm^2 Petri-dish. After freezing at -19°C for

24 h, the water was removed via freeze drying for 24 h. The resulting materials were soaked in $2 \text{ M ZnSO}_4 \cdot \text{H}_2\text{O}$ to obtain the GPEs. A GPE synthesized using a 0.8 wt% aqueous dispersion of ChNFs crosslinked with 0.25 wt% glutaraldehyde was coded as ChNF-0.8/Glu-0.25.

2.4. Current Collector Fabrication

Free-standing $200 \pm 20 \mu\text{m}$ thick nanocomposite films were prepared by the doctor blade technique setting a gap of $600 \mu\text{m}$. 500 mg of a given polymer (PLA, PCL, or PBAT) was dissolved in 15 mL of the respective solvent for 240 min at 100°C under constant stirring. Ethyl lactate was used for PCL, while dichloromethane was required for PLA and PBAT. Once the polyesters were fully dissolved, CB was added to the solution to reach concentrations of 0, 5, 10, 20, 30, and 50 wt% with respect to the polymer. The mixture was stirred for 60 min before casting it onto a flat glass substrate. After solvent evaporation, the composite films were dried at room temperature for 24 h and another 24 h at 40°C to remove the remaining solvent.

2.5. Synthesis of the Cathode Material

$\alpha\text{-MnO}_2$ was used as the cathode material. It was synthesized using a solvent-free approach according to Alfaruqi et al.^[25] KMnO_4 and $\text{Mn}(\text{CH}_3\text{COOH})_2$ powders were introduced into a 25 mL recipient and the mixture was ball milled at 30 Hz for 50 min (stoichiometric ratio $\text{KMnO}_4\text{:Mn}(\text{CH}_3\text{COOH})_2$ of 2:3). Obtained mixture was dried in an oven at 80°C for 24 h. Subsequently, the powder was bath sonicated for 3 min and washed via centrifugation at 4000 rpm for 2 min. This process was repeated five times. The resulting powder was dried again in an oven at 80°C for 24 h and was thoroughly ground using an agate mortar to obtain the active $\alpha\text{-MnO}_2$.

2.6. Full Cell Fabrication

For full-cell characterization, Swagelok-type cells were assembled with a Zn foil of 11 mm diameter as an anode. The cathode was fabricated by mixing the active material (α -MnO₂), CB, and a polyvinylidene fluoride binder at a 75:9:16 weight ratio in 2.6 mL N-methyl-2-pyrrolidone as solvent under ball milling for 50 min at room temperature (5 mL chamber, 30 Hz). The slurry was cast onto a glass substrate using doctor blade with a 500 μ m gap followed by room temperature drying for 24 h and additional drying in an air circulating oven at 40 °C for 24 h. A final thickness of 45 μ m with a mass loading of 2 mg·cm⁻² was obtained. Galvanostatic charge–discharge curves were measured at room temperature in the +0.45 to +2.00 V (versus Zn) window at current densities of 100, 200, 500, 1000, and 2000 mA·g⁻¹. For comparison, the performance of Zn/ α -MnO₂ full cells containing a glass microfibre separator soaked in 2 M ZnSO₄·H₂O was also investigated. Specific capacities and current densities were calculated based on the mass of the cathode material.

2.7. Transient Battery Fabrication

A transient ZIB was constructed using metallic zinc as the anode (280 μ m thick), α -MnO₂ as the cathode (38 μ m thick), and the ChNF-0.8/Glu-1.0 as the GPE. PBAT/CB 20 wt% films (33 μ m thick) were used as current collectors and the whole battery was encased by a 38 μ m thick PCL film. Transiency tests were conducted in ultrapure water at a temperature of 70 °C using a beaker of 70 mm diameter. The prototype for open-circuit voltage measurement has fully stacked layers, while the transient prototype has slid layers (current collectors, anode, GPE, cathode) to clearly observe the transiency of each component.

2.8. Characterization

Scanning electron microscopy (SEM) analyses were performed on a DSM 982 Gemini instrument at an acceleration voltage of 3–5 kV. For ChNF dispersion, a droplet of diluted water suspension (0.1% w/w) was deposited onto silicon wafer substrates and the resulting film was observed after room-temperature drying at 60 °C for 12 h. For GPEs, before analysis, the cryo-fractured surfaces were sputtered with a 6 nm thick platinum coating. Atomic force microscope (AFM) was used to observe the nanostructural features and topology of ChNFs. A Veeco Instrument's Multi-Mode SPM 004-130-000 AFM at room temperature was used. A droplet of ChNF suspensions (0.02% (w/w)) was coated onto a mica substrate and the water was evaporated at room temperature. The NanoScope Analysis 1.9 program was employed to analyze the recorded images. Powder X-ray diffraction (XRD) patterns were obtained with a PANalytical Empyrean powder diffractometer in reflection mode using Cu K α radiation (45 kV, 40 mA). Attenuated total reflectance Fourier transform infrared (ATR-FTIR) spectra were recorded on a Bruker Alpha FT-IR Spectrometer equipped with diamond ATR optics (2 cm⁻¹ resolution). Size distribution at neutral pH and ζ -potential as a function of pH were performed on a Malvern Zetasizer Nano-ZS using water-dispersed ChNFs at a particle concentration of 0.06

mg·mL⁻¹. The pH was tuned by titrating 0.05 mol·L⁻¹ NaOH or 0.05 mol·L⁻¹ HCl into the ChNF dispersion.

The thermodegradation of cryogels was assessed in a thermogravimetric analysis (TGA) METTLER TOLEDO 822e using alumina pans at a heating rate of 10 °C·min⁻¹ and 50 mL·min⁻¹ under air atmosphere (samples of 8 \pm 1 mg). Nitrogen sorption experiments of cryogels were performed in a Quantochrome Autosorb-iQ-C-XR at 77 K with nitrogen (99.999%) and helium (99.999%). Before analyses, the cryogels were degassed in vacuum at 60 °C for 24 h. The specific surface area was determined using the Brunauer–Emmet–Teller (BET) method. The mechanical response of the electrolyte-soaked cryogels, the GPEs, and current collector composite films was studied in a universal testing machine (Trapezium Shimadzu AGS-X) equipped with a 100 N load cell. For GPEs, compression mode tests in displacement control mode at a rate of 0.5 mm·min⁻¹ were used. Cylinder-shaped 3.0 \pm 0.2 mm thick GPEs with ϕ = 10 \pm 1 mm were used. For polyester/CB nanocomposites, uniaxial tensile tests of 30 mm long, 8 mm wide, and 200 \pm 20 μ m films were performed at a deformation rate of 2 mm·min⁻¹. The mean average value and standard deviation of Young's modulus (E) were determined from three measurements. The electrical conductivity of polyester/CB films was measured using the four-point probe method with rectangular-shaped samples.

The electrolyte uptake (EU) was measured after immersing the cryogels into 2 M ZnSO₄·H₂O for 24 h as:

$$EU = \frac{100}{m_{\text{dry}}} \times (m_{\text{wet}} - m_{\text{dry}}) \quad (1)$$

being m_{wet} and m_{dry} the weight of the wet and fully dried gels, respectively.

Electrochemical studies were carried out using a VMP3 Biologic electrochemical workstation. 13 mm diameter GPEs were assembled into Swagelok-type cells at room temperature. The electrochemical stability window was studied by voltammetric measurements with GPEs sandwiched between a titanium working electrode and a Zn metal reference/counter electrode. The voltammograms were measured in the –0.25 to +2.00 V range versus Zn/Zn²⁺ with a scan rate of 1 mV·s⁻¹. For ionic conductivity, GPEs were sandwiched between two titanium rods and the resistance was measured using a two-probe ac impedance spectroscopy analyzer with a 5 mV voltage amplitude in the frequency range from 100 mHz to 400 kHz. The bulk resistance was measured from the high frequency intercept on the real axis in the Nyquist plots, and the ionic conductivity (σ_i) was obtained as:

$$\sigma_i = \frac{d}{R_b \times A} \quad (2)$$

where d is the GPE thickness, R_b is the bulk resistance, and A accounts for the contact area of the GPE and the titanium rod.

The zinc ion transference number ($t_{\text{Zn}^{2+}}$) was determined using the Bruce–Vincent equation:^[8,20]

$$t_{\text{Zn}^{2+}} = \frac{I_{\text{ss}} (\Delta V - I_0 R_0)}{I_0 (\Delta V - I_{\text{ss}} R_{\text{ss}})} \quad (3)$$

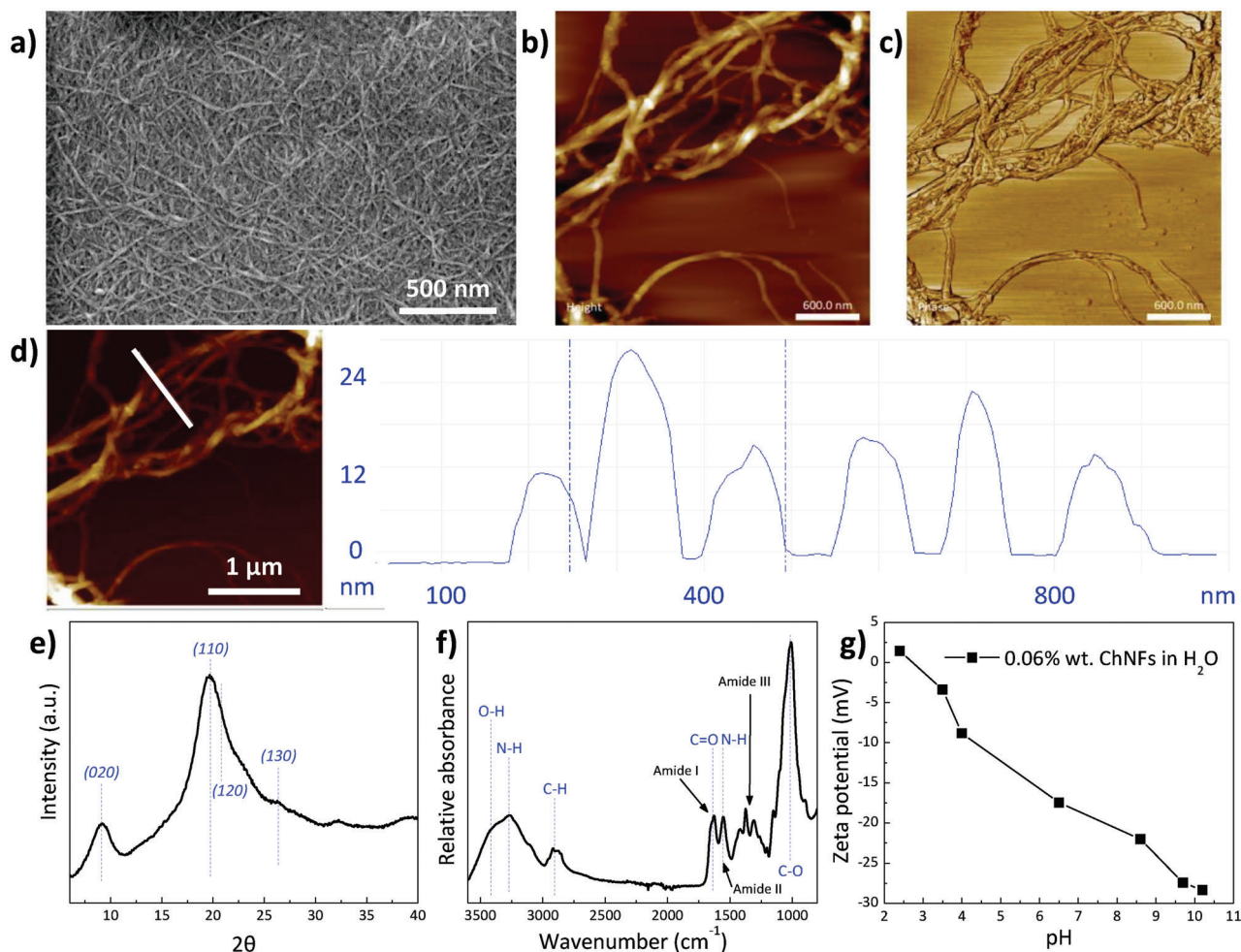


Figure 2. Morphological, structural, and conformational characterization of chitin nanofibrils as revealed by: a) SEM micrograph; b) contact-mode AFM height and c) and phase images; d) AFM cross-sectional analysis; e) XRD patterns; f) ATR-FTIR spectrum and g) zeta-potential at varying pH.

where I_0 and I_{ss} are the currents in the non-polarized and polarized states, respectively, R_0 and R_{ss} are the resistances in the non-polarized and polarized states, respectively, and ΔV accounts for the applied potential step. GPEs were mounted in a symmetric Swagelok-type cell between two Zn foils. 30 mV was applied in DC mode for 1 h, and the impedance spectroscopy data were recorded before and after the polarization in the 100 kHz–100 MHz frequency range with an AC perturbation of 5 mV.

Zn stripping and plating were studied at varying current densities from ± 0.8 to ± 9.5 mA·cm⁻² using GPEs mounted between two Zn-metal discs. For comparison, Zn stripping and plating were also performed using a glass fiber separator soaked in 2 M ZnSO₄·H₂O. For post-mortem SEM studies, the cycled Zn surfaces were washed with water before drying under vacuum.

3. Results and Discussion

3.1. ChNFs Characterization

First, we characterized the morphological features of ChNFs extracted from white mushroom (*Agaricus bisporus*), and the results

are summarized in **Figure 2a** by SEM. Upon casting of a 0.1% w/w ChNF water drop, the self-assembly process results in the formation of a thin and isotropic film composed of fibrillar-like long and flexible nanowires matching with the previous observations by Bismarck et al.^[17] AFM images in **Figure 2b–d** provide additional details on the nanostructure and the 3D surface topology of the fibrils. The representative AFM height and phase images show the thin and fibrillar-like character of ChNFs, which entangle into larger bundles consisting of 10–20 nanofibrils. According to the AFM images, the lengths of the nanofibrils extend over several microns. A cross-sectional analysis shows a narrow distribution of the width of ChNFs with a dimension of 100.4 ± 8.7 nm (based on 20 counts). These values are similar to previous reports on ChNFs isolated from crab shells using 2 M HCl, where diameters of particle-aggregates from 70 to 150 nm were observed.^[26] The average hydrodynamic particle size obtained by dynamic light scattering in **Figure S1**, Supporting Information confirms the sub-micrometer character of ChNFs, matching with morphological observations by SEM and AFM. As single α -chitin crystallites are notably smaller with diameters of 2–5 nm and lengths of ≈ 300 nm (usually composed upon the

arrangement of 18–25 chitin molecular chains having an anti-parallel alignment),^[27] it is reasonable to argue that the individual fibrils isolated from fungi (diameters around 100 nm) are composite structures containing α -chitin crystallites bonded by glucans (further evidenced in the following sections).^[17,28]

The structure and conformational features of ChNFs were further explored by XRD and ATR-FTIR experiments, respectively. Isolated ChNFs combine both crystalline and amorphous regions as revealed by the XRD pattern in Figure 2e. The amorphous halo originates from the presence of β -glucans on the ChNFs surfaces,^[17] while the broad peaks located at $2\theta = 9.2^\circ$ and 19.7° , the shoulder at $2\theta = 20.5^\circ$, and the weaker peak at $2\theta = 26.2^\circ$ are assigned to (020), (110), (120) and (130) crystal planes, respectively, confirming the presence of crystalline α -chitin organized into a 2-chain orthorhombic unit cell.^[29] According to Bragg's law, the interplanar spacing ($d_{hkl} = \lambda/2 \cdot \sin\theta$) values corresponding to the (020) and (110) planes are ≈ 9.61 and ≈ 4.51 Å, respectively. These values remain below the 9.70–9.78 Å and 4.63–4.65 Å reported for chitin microcrystals extracted from Antarctic krill, crab, and shrimp shells upon HCl hydrolysis.^[30] Thus, we conclude that the mild ChNF extraction process here applied does not disrupt the hydrogen bonding within the chitin crystallites (as the crystalline order is kept), ensuring a higher quality of nanofibrils when compared with nanochitin extracted from crustacean exoskeletons, which require extensive demineralization and deproteination steps with notable environmental burdens.^[18]

As chitin chains interact via H-bonding between amine and carbonyl groups depending on the crystalline polymorphs (namely α -, β -, and γ -chitin), FTIR spectroscopy is a quick yet accurate technique to determine the packing mode of chitin chains.^[29] The FTIR spectrum in Figure 2f shows the characteristic absorption bands of chitin, with a broad band in the 3650–3200 cm^{-1} region originating from the –OH stretching at 3434 cm^{-1} and the –NH stretching at 3276 cm^{-1} , together with the bands at 2911 and 2841 cm^{-1} from the –CH groups, and the amide I, amide II and amide III bands centered at 1628, 1556, and 1315 cm^{-1} , respectively. A doublet is observed in the C=O stretching amide I band, which indicates the presence of α -chitin polymorph (as opposed to the α form, β form presents a single band at 1640 cm^{-1} due to the hydrogen bonds between the molecules).^[29] The doublet is observed in a convoluted form because of the presence of amorphous glucans, which is composed of glucose and other sugars as shown in Figure S2, Supporting Information.^[31] The sharp peaks appearing at 1378 and 1029 cm^{-1} are due to the CH₃ symmetrical deformation and C–O–C groups in chitin, respectively.^[32] The presence of the secondary amide groups in chitin (as opposed to the primary amide of chitosan) is verified by the presence of the amide III absorption band. In addition, the shoulder appearing at 3105 cm^{-1} indicates the presence of secondary amines of α -chitin.^[30] The stretching vibration of proteins at 1540 cm^{-1} is absent, indicating their complete removal.^[33] The fact that the relative intensity of the amide bands is reduced in comparison with chitin nanocrystals from crustaceans shells is explained by the presence of covalently bonded β -glucan (≈ 40 wt% of the total composition)^[32] surrounding the crystalline chitin regions as schematically illustrated in Figure S3, Supporting Information (hydrophobin and melanin are also present according to our envisaged structure as will be discussed later). This β -glucan lowers the overall nitrogen con-

tent to 3.07 ± 0.01 wt% (43.23 ± 0.12 wt% for carbon, 6.41 ± 0.05 wt% for hydrogen) in comparison with the 6.89 wt% nitrogen found in chitin (47.29 wt% for carbon, 6.45 wt% for hydrogen) as confirmed by the CHN elemental analysis. To understand the effect of the ChNF surface charge under different environments and its interaction with electrolytes, the ζ -potential of a 0.06 wt% ChNFs dispersion in water from acidic to alkaline conditions was studied. The isoelectric point is found at a pH close to 2.7 (Figure 2g). Under very acidic environments, the *N*-acetyl groups of ChNFs remain protonated so their potential is slightly positive (1.43 mV at pH 2.4). This small value originates from the low fraction of amine groups when compared with raw nanochitin (N content in ChNF is as low as 3.8 wt%, while the N content for chitin from crustaceans is 6.5 wt%).^[34] Increasing the pH leads to negative values that reach -21.5 ± 2.4 mV at pH 8, very similar to the -21 mV previously reported.^[32] These results indicate that the dissociable carboxylic acid groups onto ChNFs become fully deprotonated under neutral and acidic environments. It is important to note that when soaked into the aqueous 2 M ZnSO₄ electrolyte, the ChNF GPE may show a slightly negative charge as the electrolyte pH is around 4.5.^[4]

3.2. Gel Morphology and Physico-Chemical Properties

The structural flexibility and the high aspect-ratio morphology of ChNFs facilitate their interaction, deformation, and entanglement into gels.^[19] These features contrast with the rod-like shape of chitin nanocrystals that are 5–50 nm wide and 150–2200 nm long extracted upon hydrolysis of crustacean shells by strongly acidic aqueous solutions.^[35,36] Therefore, it may be possible to exploit ChNFs to achieve low overlap concentrations, that is, the minimum concentration needed to render particle-particle interactions.^[37,38] Accordingly, we prepared porous structures that are expected to facilitate a rapid and homogeneous Zn²⁺ transfer. We followed a bottom-up approach, in which hydrogels are prepared by chemical cross-linking of ChNFs with different concentrations in water using glutaraldehyde. Cross-linking is an essential step to get mechanically resilient gels and prevent individual nanofibril re-dispersion once the gels get in contact with liquids. The hydrated and cross-linked 3D networks are converted into cryogels by removing the aqueous liquid phase through freeze-drying. We used these cryogels to obtain GPEs after infiltration of 2 M ZnSO₄·H₂O via capillary effects. Figure S4, Supporting Information shows the macroscopic appearance of the GPEs, where the brown color of the gels results from the presence of the pigment melanin in fungi (as indicated by the small C–N stretching peak at 1460–1400 cm^{-1} in Figure 2f originating from the indole structure of melanin).^[17]

Figure 3a represents the cross-sectional SEM micrographs of ChNF cryogels. Obtained pore-sizes are optimal to facilitate a stable and homogeneous ion flux across the electrolyte, avoiding undesired ion concentration gradients that contribute to cell polarization, thus limiting the risk of dendrite formation.^[39] The interconnected porous network structure occurring for all the compositions provides a continuous liquid phase and ensures extended ion migration pathways in the electrolyte.^[40] The SEM images in Figure S5, Supporting Information show that self-assembled ChNFs form the wall of these pores. These results are particularly

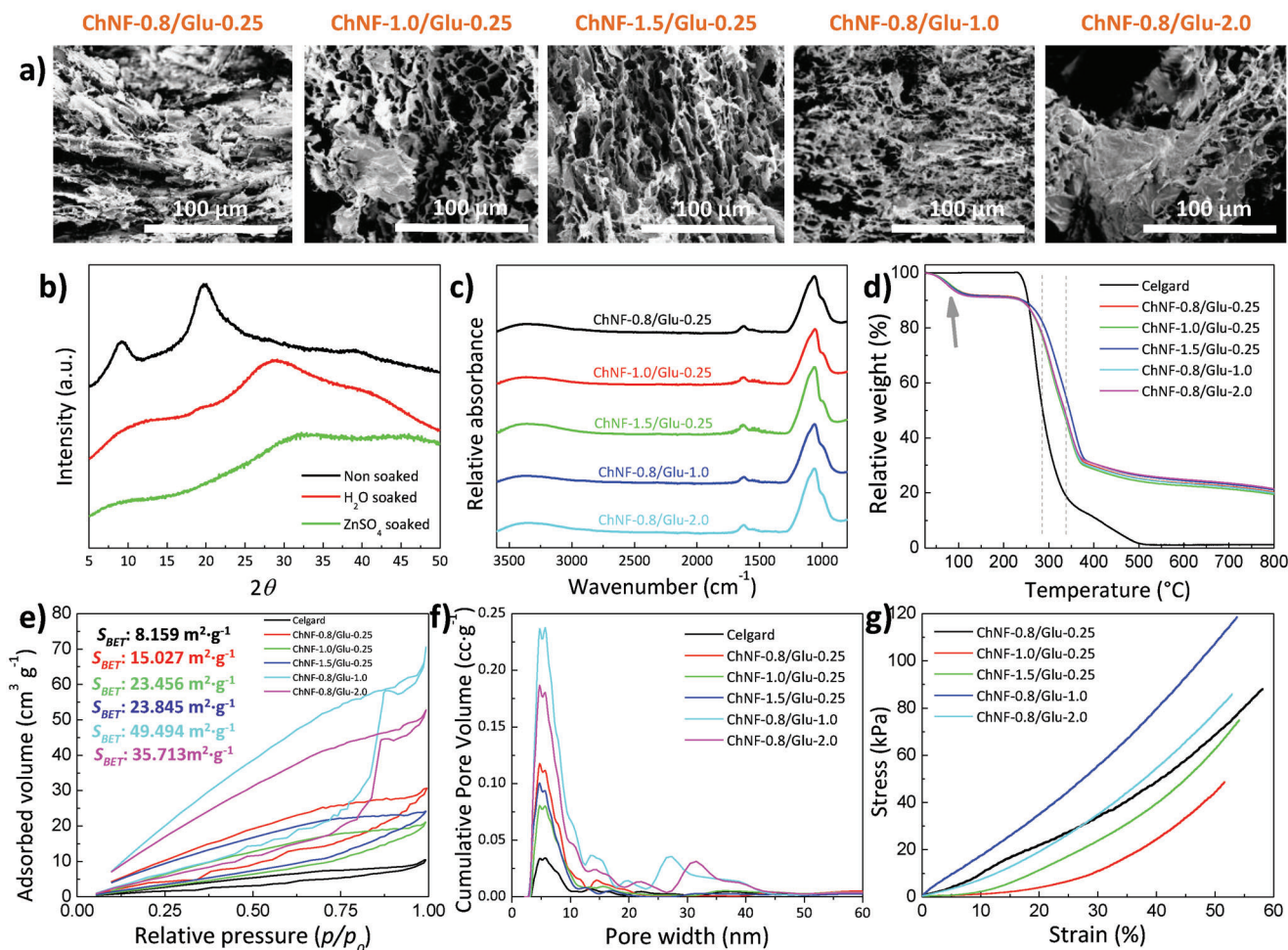


Figure 3. a) Representative SEM micrographs showing the cross section of ChNF-based cryogels at different ChNF:water and ChNF:glutaraldehyde ratios. b) XRD patterns of ChNF-1.0/Glu-0.25 cryogel, and H₂O and 2 M ZnSO₄·H₂O-soaked GPEs; c) ATR-FTIR spectra; d) thermogravimetric traces; e) N₂ adsorption–desorption isotherms; f) DFT pore size distribution of freeze-dried CNC/CNF cryogels; g) representative stress–strain curves of the GPEs compressed in the transverse direction.

promising considering the remarkably low amount of ChNFs needed to obtain gels (0.8 wt%), which maximizes the porosity and the isotropic arrangement of the pores. For comparison, a recent work by our group has shown that 4 and 2 wt% are required to obtain free-standing gels with cellulose nanocrystals and cellulose nanofibrils, respectively.^[8] The low biocolloid concentration required for gel formation is a result of the flexible character of ChNFs facilitating the formation of physically entangled structures. The abundant functional groups on the nanofibril surfaces offer maximum exposure to interact and dissociate zinc salts upon soaking in 2 M ZnSO₄·H₂O.

The developed cryogels are predominantly amorphous with the coexistence of a crystalline phase as confirmed by the broad diffraction peaks originating from chitin together with a broad amorphous halo in Figure 3b. Soaking the cryogels into H₂O or 2 M ZnSO₄·H₂O further lowers their crystalline character, suggesting that the water reduces the intermolecular interactions between the chitin chains to yield predominantly amorphous GPEs, a feature commonly related to favoring ion diffusivity.^[5] In addition, no peaks corresponding to ZnSO₄ are present in the XRD

patterns, suggesting the formation of a polymer–salt complex between Zn²⁺ and the functional groups of ChNFs.^[41] This observation sharply contrasts with the results observed in petroleum-based GPEs (poly(vinyl alcohol)), where zinc salts easily precipitate and fail to form highly ionically conducting materials.^[42,43] ATR-FTIR spectra in Figure 3c and Figure S6, Supporting Information show that after glutaraldehyde cross-linking, the sharp amide I bands (at 1655 and 1620 cm⁻¹) transform into a single and broad absorption band centered at 1630 cm⁻¹ as a result of the formation of acetal bridges.^[44] In addition, the bands at 2800–3600 cm⁻¹ lose intensity after cross-linking due to the reduced concentrations of the –OH, –NH, and –CH groups left after the cross-linking reaction.^[45] When comparing with neat ChNFs (Figure 2f), a new shoulder emerges at ≈981 cm⁻¹ originating from the sulfate ion for all the cryogels soaked in the liquid electrolyte,^[41] confirming an efficient salt dissociation (into Zn²⁺ and SO₄²⁻ ions) in the GPEs.

The thermal stability of the fabricated materials was assessed given its relevance toward safe batteries. An improved thermal stability may protect the battery against undesired thermal run-

away and associated fire and explosion events.^[46] Figure 3d shows the TGA curves of the cryogels. As opposed to the marked weight loss event occurring for Celgard, ChNF-based cryogels present an initial loss of ≈ 8 wt% associated with adsorbed water (centered at 80 °C, grey arrow), followed by ≈ 60 wt% loss in the 245–380 °C range originating from the degradation of 2-amino-2-deoxy-*D*-glucopyranose units. Finally, a 21 wt% char equivalent is obtained at 800 °C. We found that the *N*-acetylated units in the cryogels are responsible for enhancing the $T_{50\%}$ (determined by the 50 wt% loss) by ≈ 55 °C when comparing with Celgard separator, or by ≈ 37 °C when comparing with nanocellulose-GPEs.^[8] Figure 3e depicts the N_2 adsorption–desorption isotherms of freeze-dried ChNF cryogels, from which BET surface areas (S_{BET}) in the range of 15.0 to 49.5 $\text{m}^2\cdot\text{g}^{-1}$ are extracted. These values represent, to the best of our knowledge, the largest specific surface areas reported so far for ChNF-based structures, including the 0.22 $\text{m}^2\cdot\text{g}^{-1}$ reported for ChNF nanopapers.^[34] In addition, the increased specific surface area compared to the low surface area of 8.2 $\text{m}^2\cdot\text{g}^{-1}$ measured for Celgard offers significantly more sites to interact with the liquid electrolyte, which in turn may be translated into a facilitated ion diffusion. As shown by the DFT pore size distribution in Figure 3f, the mesopores within the 4 to 10 nm range notably contribute to the pore volume of ChNF. Such mesoporosity, in combination with the micron-sized pores observed by electron microscopy in Figure 3 proves the hierarchical structure of the gels. These characteristics provide an ideal architecture for homogeneous Zn^{2+} diffusion across the electrolyte.^[47]

The mechanical response of the GPEs under uniaxial compression was measured to evaluate their potentiality to provide good interfacial contact with electrodes (elasticity) and physical barrier against undesired dendrite growth (stiffness). Representative compressive stress–strain curves in Figure 3g depict an elastic behavior at low deformations (<12%), followed by a plastic deformation region at larger strains.^[48] The compressive modulus increases from 72.4 kPa for the ChNF-0.8/Glu-0.25 GPE to 182.3 kPa upon cross-linking with 1 wt% glutaraldehyde (Figure S7a, Supporting Information). However, a larger cross-linker concentration lowers the modulus to 59.3 kPa, suggesting that there is an optimal glutaraldehyde concentration to provide a robust 3D network capable to resist externally induced compressive forces. The obtained modulus values ranging from 59.3 to 182.3 kPa are well-above the 7 kPa showed by cellulose nanocrystal aerogels soaked into 1 M Na_2SO_4 .^[49] We attribute such large values to the glucan, which enhances the binding between individual crystalline nanochitin (as shown in Figure S3, Supporting Information).^[17] Surprisingly, a ChNF concentration increases to 1 or 1.5 wt% results in a pronounced modulus decrease to values of 7.2–9.7 kPa (a similar trend is observed for the strength at 50% strain in Figure S7b, Supporting Information). Besides, the stress–strain curves corresponding to five loading–unloading cycles compressed to 50% of their original thickness in Figure S8, Supporting Information show a good resistance to cyclic fatigue damage as indicated by the small reduction of the stress–strain hysteresis after successive cycles (i.e., the progressive structural damage known as shakedown is limited).^[50] The quantification of the area (Figure S9, Supporting Information) within the loading–unloading loops indicates an enhanced reversibility for the ChNF-0.8/Glu-0.25 GPE. On the contrary, large cross-linker concentrations make the gel stiffer, decreasing its

capacity to accommodate external stresses without deformation. Overall, we ascribe the good compressive cycling stability to the highly porous and stable 3D ChNF skeleton cross-linked by acetal bridges, which in addition presents an increased binding between individual nanofibrils provided by the glucans.^[17]

3.3. Electrochemical Characterization

The hierarchical porous structure of the cryogels observed by SEM, together with the mechanical properties of the hydrogels, make these materials good contenders to act as GPEs in batteries. We thus immersed the cryogels into a 2 M ZnSO_4 electrolyte and observed a quick absorption and retention of the liquid. As such, an EU up to 4046% was achieved for the ChNF-0.8/Glu-0.25 cryogel (Figure 4a). Cross-linker concentration increase barely affects the EU, while ChNF concentration increase notably lowers EU to a minimum of 1527%. In any case, the obtained values are well above the EU shown by the glass microfibre separator (906%). Obtained EU values are remarkable considering that the ChNFs derived from fungi have a relatively low concentration of polar amine/amide groups compared to crustacean-derived nanochitin or nanocelluloses.^[34] Additionally, the presence of the hydrophobic hydrophobins (see Figure S3, Supporting Information), which are cysteine-rich proteins found only in filamentous fungi and mushrooms, may also reduce the electrolyte wettability of the gel. Therefore, it seems that the gel architecture plays a pivotal role. As such, the interconnected 3D mesopores of the gels facilitate EU and retention by capillary forces.^[8] In addition, amorphous β -glucans promote water penetration in comparison with highly crystalline (crystallinity degrees above 80%) chitin nanoparticles extracted through conventional routes.^[17]

As the electrochemical stability of the electrolyte determines its operating range, voltammetric measurements in the potential range of -0.25 – 2.0 V versus Zn/Zn^{2+} were performed. A high anodic stability reaching 2.0 V versus Zn/Zn^{2+} is observed as indicated by the flat lines at high voltages in Figure 4b, allowing the implementation of ChNF-based GPEs in high-voltage ZIB configurations. Reversible zinc deposition and dissolution currents are observed, where the intensity of the anodic and cathodic peaks decreases with increasing ChNF concentration in the GPE (for the lower glutaraldehyde concentration). Larger amounts of crosslinker increase the intensity of the anodic and cathodic peaks, suggesting an increased resistance to Zn dissolution/deposition process.^[51] Based on the Nyquist impedance plots in Figure 4c, the ionic conductivity of the GPEs is determined and summarized in Figure 4d. All the samples present straight lines with no semicircles, indicating the ionically conducting nature of the membranes. A maximum conductivity of 54.1 $\text{mS}\cdot\text{cm}^{-1}$ is obtained for the ChNF-0.8/Glu-2.0 GPE, exceeding the conductivities of a few $\text{mS}\cdot\text{cm}^{-1}$ required for practical applications. They are above the value observed for the glass microfibre separator soaked with the liquid electrolyte (31.8 $\text{mS}\cdot\text{cm}^{-1}$). Comparing with the conductivity of 21.1 $\text{mS}\cdot\text{cm}^{-1}$ observed for the ChNF-0.8/Glu-0.25 GPE, the ionic conductivity decreases to a minimum of 11.3 $\text{mS}\cdot\text{cm}^{-1}$ for the ChNF-1.5/Glu-0.25 GPE (larger ChNF concentration), and increases to a maximum of 54.1 $\text{mS}\cdot\text{cm}^{-1}$ for the ChNF-0.8/Glu-2.0 Glu GPE (larger glutaraldehyde concentration). These results are particularly

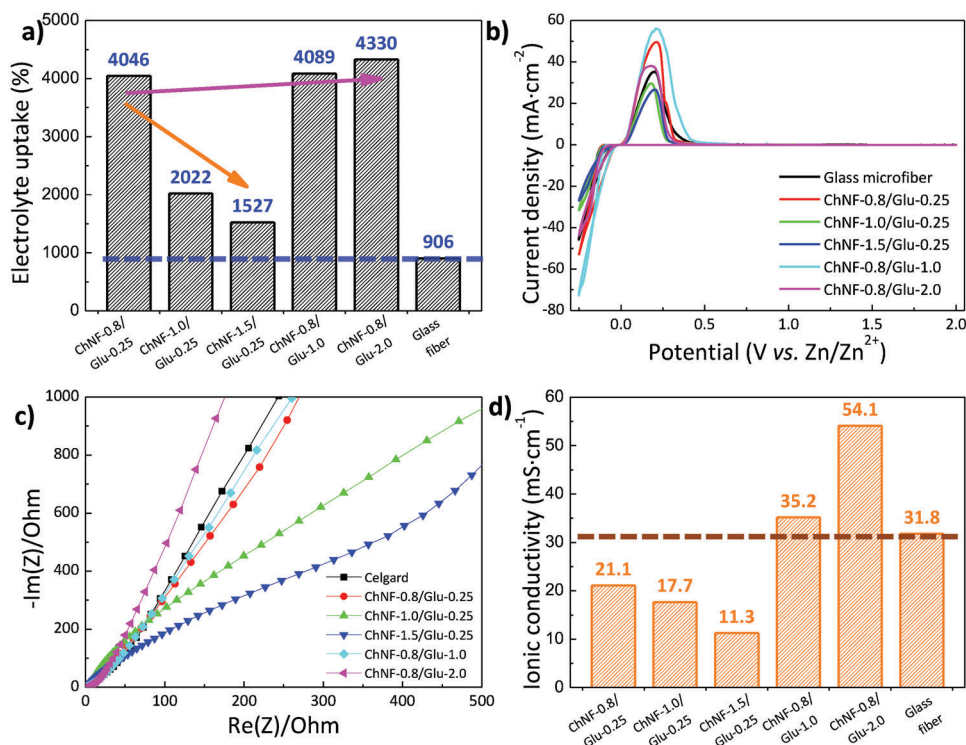


Figure 4. a) Electrolyte uptake; b) electrochemical stability window at a sweep rate of 1 mV·s⁻¹ (tested within the conventional range of interest in ZIBs) and c) Nyquist impedance plots and d) Zn²⁺ conductivity of ChNF-based GPEs. Data corresponding to a glass fiber separator soaked in 2 M ZnSO₄·H₂O is shown as a reference.

relevant considering our ionic conductivities also outperform the majority of values reported for GPEs applied in ZIBs, including the 0.12 mS·cm⁻¹ showed by carboxymethyl cellulose/ZnSO₄ GPEs,^[41] the 16.4 mS·cm⁻¹ of a cellulose nanofibril GPE,^[52] or the 8.9 mS·cm⁻¹ of chitosan/choline nitrate GPEs.^[53] It is noted that increased conductivities are achieved upon reducing ChNF concentration or increasing glutaraldehyde concentration. These results are in line with previous reports on polymer electrolytes from natural origin (such as alginate), where additional ion migration pathways to increase ionic conductivity over petroleum-based polymers such as poly(ethylene oxide),^[40] or poly(vinyl alcohol) have been observed.^[54] The following aspects may play a determinant role in reaching such large ionic conductivities.

- The mostly amorphous character of the GPEs does not impede Zn²⁺ migration through the electrolyte.^[5,6]
- The interconnected 3D porous structure of the gels facilitates a uniform ion transport in the GPEs,^[8] supporting water-retention (EU values of 1527–4046%) and providing large amounts of liquid solvents to facilitate Zn²⁺ motion through the mobile liquid phase.^[6,39]
- The abundant oxygen-containing groups in chitin and β-glucan interact with Zn²⁺ to boost ion hopping around the continuous polymeric backbone, which in turn enhances ion migration and diffusion pathways.^[8,40]
- The presence of β-glucans lowers hydrogen bonding between adjacent chitin chains, forming an interpenetrating polymer network with increased Zn²⁺ conductivity.^[54]

- Oxygen atoms from glucose units in chitin can coordinate with Zn²⁺ to facilitate its solvation, thus shortening conduction pathways.^[55]
- Larger glutaraldehyde concentrations provide additional hydrophilic acetal linkages (in comparison with low crosslinking ratios) facilitating EU and thus, the Zn²⁺ conduction process.^[56]

Further insights on the ion conductivity were obtained upon the determination of the zinc ion transference number ($t_{Zn^{2+}}$) according to the Bruce–Vincent method.^[8,20] As depicted in the chronoamperometry profiles of Figure S10, Supporting Information, a maximum ($t_{Zn^{2+}}$) of 0.468 is achieved for the ChNF-1.5/Glu-0.25 GPE. The transference number nearly doubles by increasing the ChNF concentration from 0.8 to 1.5 wt%, similar to what occurs with Na⁺ conducting cellulose nanofibril GPEs.^[8] This trend suggests that the ChNF surface chemistry (with abundant oxygen-containing groups) strongly interacts with the ZnSO₄ salt in the electrolyte, facilitating ion pair dissociation into Zn²⁺ and SO₄²⁻ and thus improving the Zn ion transport. As a consequence, the further ChNF surfaces exposed to interact with the zinc salt, the larger $t_{Zn^{2+}}$ results.

After noting that ChNF-based GPEs offer a wide electrochemical stability window and a competitive ionic conductivity, we explored the long-term stability of the Zn²⁺ electrodeposition as a next prerequisite toward high-performance ZIBs. Symmetric Zn/Zn cells were assembled to conduct plating and stripping experiments at areal current densities ranging from ± 0.8 to ± 9.5 mA·cm⁻² and the results are summarized in Figure 5. All the

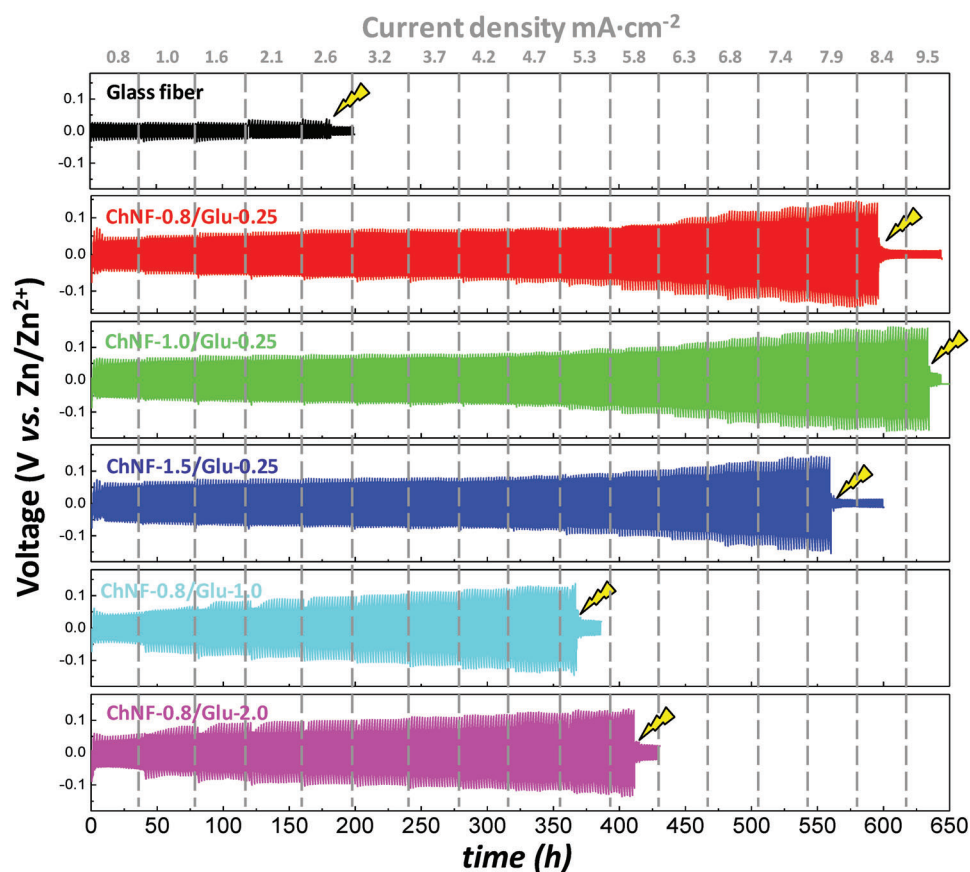


Figure 5. Room temperature voltage–time profiles for the symmetric Zn plating–stripping at areal current densities from $\pm 0.8 \text{ mA}\cdot\text{cm}^{-2}$ to $\pm 9.5 \text{ mA}\cdot\text{cm}^{-2}$ for a glass fiber soaked in $2 \text{ M ZnSO}_4\cdot\text{H}_2\text{O}$ and the ChNF-based GPEs (the lightning symbol marks the occurrence of short circuit).

samples present an increasing overpotential with applied current density. For a given current density and among the studied compositions, the ChNF-0.8/Glu-0.25 GPE shows the lowest overpotential values of 136 mV (magnified voltage versus time curves at $\pm 4.2 \text{ mA}\cdot\text{cm}^{-2}$ are shown in Figure S11, Supporting Information), indicating an improved reversibility of the Zn^{2+} transport through the gels and homogeneous Zn metal electrodeposition. The overpotential remains barely unchanged upon increasing the ChNF concentration in the GPE, but scales up to 221 and 238 mV at glutaraldehyde concentrations of 1.0 and 2.0 wt%, respectively. These results are ascribed to a homogeneous Zn^{2+} transport across the electrodes minimizing polarization losses and suppressing ionic concentration gradients at high current densities. Besides, the square-shape polarization curve shown by the GPEs becomes distorted with increasing cross-linker concentration, indicating a smoother Zn deposition and lower tortuosity within the GPE for Zn^{2+} transport provided by the hierarchically ordered mesoporous architecture of the gels with low cross-linking.^[8] Similarly, the sudden voltage drop (indicated by the lightning symbol) is delayed to a maximum of $\pm 9.5 \text{ mA}\cdot\text{cm}^{-2}$ (634 h) for the ChNF-0.8/Glu-0.25 GPE compared to premature short-circuit at $\pm 5.3 \text{ mA}\cdot\text{cm}^{-2}$ (367 h) or $\pm 2.6 \text{ mA}\cdot\text{cm}^{-2}$ (175 h) when cross-linker concentration increases, or when the glass microfibre is used, respectively.

Post-mortem SEM analyses of cycled Zn surfaces in Figure S12, Supporting Information, and the corresponding EDX results in Figure S13, Supporting Information show a hexagonally close-packed orientated texture for the ChNF-0.8/Glu-0.25 GPE, in contrast to the uneven morphology when glass microfibre is used as a separator. This hexagonal zinc texture with a parallel alignment to the Zn surface can be correlated to the growth of Zn along the (002) plane during Zn^{2+} deposition. In contrast, a non-uniform Zn growth is realized when the glass microfibre separator soaked into the liquid electrolyte is used (Figure S14, Supporting Information). It seems that ChNF GPEs have the ability to texture the Zn^{2+} nucleation and deposition to a plane with a high activation energy for Zn dissolution but that resists side reactions to prevent dendrite formation and thus results in a prolonged battery lifespan. In the case of the microporous glass fiber separator, the electrodeposited Zn nucleates along the vertically aligned (to the Zn surface) (101) and (110) crystal planes for zinc supporting dendrite growth.^[57] The atomic percentage determination in Table S1, Supporting Information indicates a larger concentration of Zn when the ChNF-based GPEs are used. Besides, a twofold decrease on the sulfur content occurs for the Zn anode cycled with the ChNF-based GPEs. We ascribe these results to a facilitated transport of Zn^{2+} by the chitin gels. When glass microfibre is used as a separator, the oxidized metallic Zn during discharge

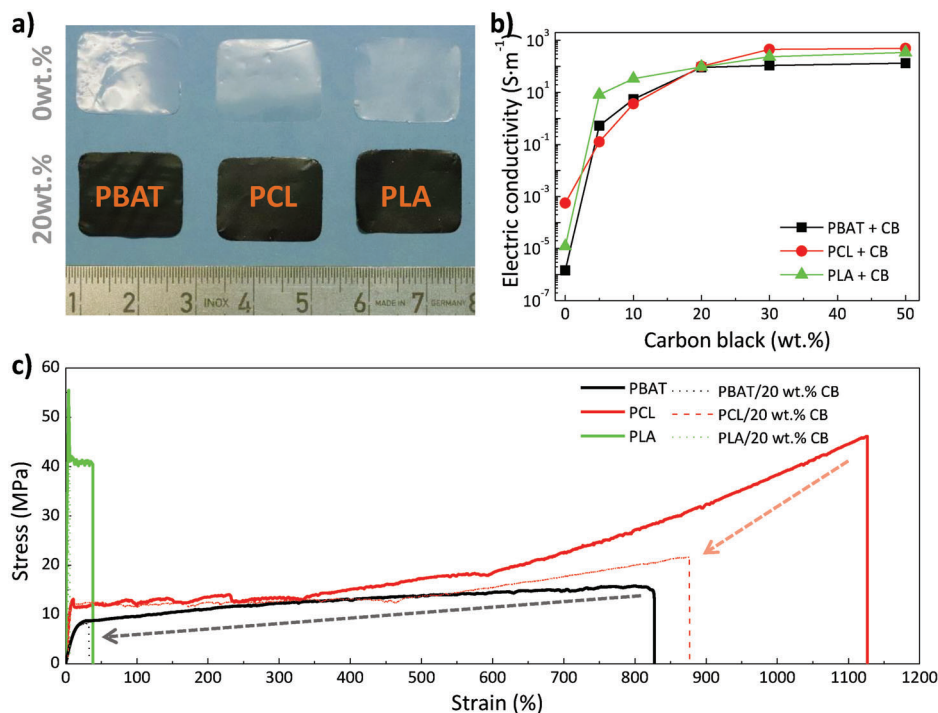


Figure 6. a) Digital photographs showing the macroscopic appearance of PBAT, PCL, PLA, and the corresponding nanocomposites with 20 wt% CB. b) Bulk electrical conductivities of PBAT-, PCL-, and PLA-CB nanocomposites. c) Representative uniaxial stress–strain curves for neat PBAT, PCL, PLA, and the corresponding nanocomposites with 20 wt% CB.

attracts OH⁻ and SO₄²⁻ anions from the liquid electrolyte to yield electrochemical corrosion products that consume the active material and deteriorate battery performance.^[58]

Besides the interconnected hierarchical porous structure of the gels, large EU, and high ionic conductivities, two further aspects may play a determinant role in achieving such electrochemical performance. First, the good mechanical adaptability of GPEs, which shows no collapse upon compression and shape-recovery after release, improves the adhesion and interfacial compatibility with Zn surfaces,^[5] and ensures optimal charge transfer between negative and positive electrodes. Second, according to a recent report from MacLachlan group studying the chitin nanocrystal-water interfaces at the single-chain level, water molecules form a stable and well-ordered hydration layer on the chitin surfaces.^[59] Therefore, we postulate that the GPEs based on ChNFs from fungi are able to strongly interact with the retained water within the porous network, avoiding the likelihood of free water molecules to cause parasitic reactions.^[60]

It is to note that the obtained combination of low overpotential, which ensures an improved active material utilization,^[61] with long lifespans, represents a significant advancement regarding GPEs applied in ZIBs, confirming that our design using biocolloids for the bottom-up fabrication of GPEs avoids a premature cell failure due to Zn dendrite-induced short-circuit.

3.4. Current Collector Fabrication

Conventionally, copper current collectors are applied in electrodes of ZIBs.^[62] This material is expensive, presents serious

supply chain issues, and degrades very slowly via corrosion reactions, making the batteries hardly biodegradable.^[21] Besides, the high density of Cu (8.96 g·cm⁻³) lowers the specific energy density of the battery. Thus, we aimed at producing biodegradable current collectors with competitive electric conductivity and tensile properties to potentially replace these materials. Given their balance between low density of ≈1.2 g·cm⁻³, thermo-mechanical performance, and biodegradability into non-toxic products, we focus our attention on biodegradable polyesters as current collectors. Using the doctor blade technique, homogeneous free-standing nanocomposite films based on PBAT, PCL, and PLA exceeding 100 cm² were fabricated (Figure S15, Supporting Information). As shown in **Figure 6a**, neat polymer films are translucent, while CB incorporation makes these materials black in appearance. CB is selected given its ability to improve the electrochemical performance of LIB current collectors by enhancing the interfacial adhesion and preventing the corrosion of pure metallic current collectors.^[63] The electrical conductivity obtained by the four-point probe method of polyester/CB nanocomposites bearing 0, 5, 10, 20, 30, and 50 wt% CB is shown in Figure 6b. Neat polyesters present an electrically insulating character with a dc conductivity below 10⁻⁴ S·m⁻¹. On the contrary, a 20 wt% CB addition increases the conductivity by 6–8 orders of magnitude with respect to neat polymers. This behavior originates from the formation of an electrically conducting 3D network that allows electrons to move through the composite material.^[64] Based on these results, the 20 wt% nanocomposites were selected to fabricate current collectors (PBAT/20 wt% CB: 134.5 S·m⁻¹; PCL/20 wt% CB: 494.8 S·m⁻¹; PLA/20 wt% CB: 343.6 S·m⁻¹). Although the obtained conductivities remain below the 5.96 ×

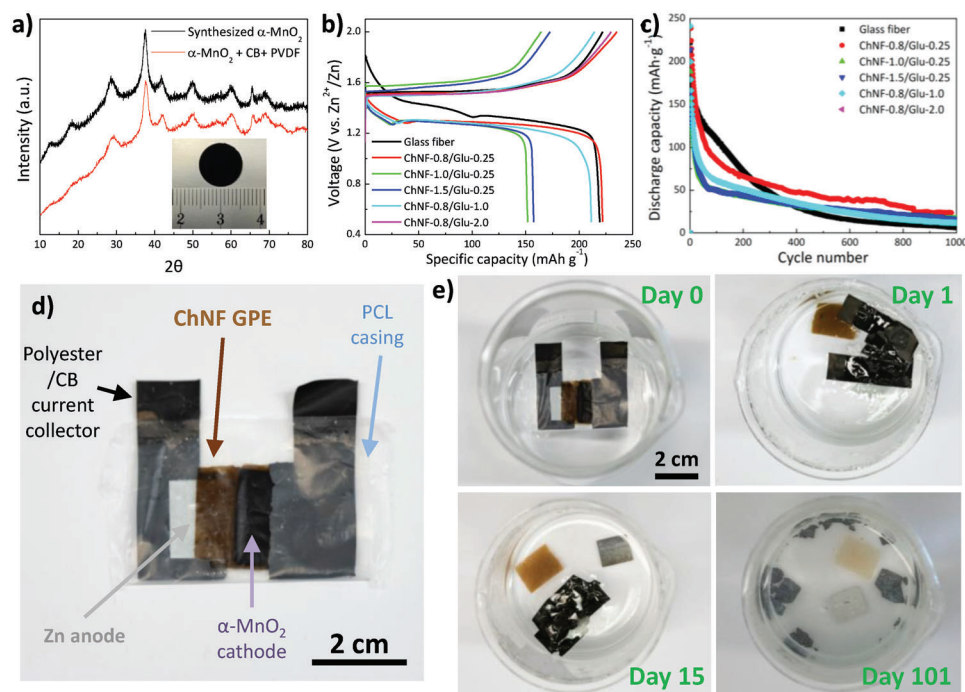


Figure 7. a) XRD patterns of as-synthesized α -MnO₂ and the prepared composite cathode. The inset shows an optical photograph of the 45 μ m thick composite cathode comprising α -MnO₂, CB, and polyvinylidene fluoride. b) First galvanostatic charge/discharge profile at 100 mA·g⁻¹ for ChNF-based GPEs and the corresponding evolution of the c) discharge capacity over 1000 cycles. Note that data corresponding to ChNF-0.8/Glu-2.0 was not obtained because of a failure due to an internal short circuit upon assembly. d) Optical photograph of the fabricated transient ZIB (Zn/ α -MnO₂ system) prototype with ChNF-0.8/Glu-1.0 GPE and e) its degradation upon immersion in ultrapure water at 70 °C (pH of 5.9) at different time periods.

10⁷ S·m⁻¹ of copper,^[62] our values approach the conductivities of carbon-based current collectors applied in industrial primary Zn-MnO₂ batteries,^[65] indicating their suitability.

In addition, current collectors should ideally be mechanically stiff but also ductile in order to keep the bonding of the active electrode materials to the current collector while ensuring an adequate integrity of the battery upon cycling.^[66] Figure 6c summarizes the representative tensile stress–strain curves for the selected compositions performed over dog bone shaped specimens according to ASTM D638 (Figure S16, Supporting Information). Neat PBAT and PCL display a ductile behavior with an elongation at break of 825 and 1126%, respectively (see the main representative parameters of tensile tests in Table S2, Supporting Information). On the contrary, neat PLA is a stiff and relatively brittle material with an elongation at break of 38.4%. Overall, CB incorporation increases Young's modulus at expenses of ductility as commonly observed in polymer nanocomposites.^[67] The modulus enhancement is particularly large for the PCL/20 wt% CB and PLA/20 wt% CB formulations, with increases from 240 ± 17 to 394 ± 36 MPa and from 1492 ± 28 to 2136 ± 191 MPa, respectively. In spite of the observed embrittlement, the samples containing 20 wt% present a sufficient malleability and ductility to function as current collector. Overall, the PCL/20 wt% CB film seems to be the most appropriate considering its balance between electric conductivity (494.8 S·m⁻¹), strength (13 ± 1 MPa stress at yield), and ductility (elongation at break above 850%). In addition, this material can be processed using the environmentally benign ethyl lactate as solvent (adhering to three principles of Green Chemistry, namely less hazardous synthesis, be-

nign solvents, and safer processes),^[68] as opposed to the carcinogenic chloroform required for PLA and PBAT (ethyl lactate failed to provide pore-free films). Importantly, ethyl lactate can be obtained upon post-consumer PLA-waste upcycling under mild reaction conditions,^[69] offering an environmentally benign solvent to transition toward circular patterns.

3.5. Battery Performance and Transiency

After optimization of porosity, mechanical properties, EU, electrochemical stability window, ionic conductivity, and Zn²⁺ electrodeposition stability, the potential of ChNF GPEs as a ZIB electrolyte was evaluated. α -MnO₂ was selected as an electrochemically competitive and environmentally sustainable cathode (avoiding genotoxic and scarce vanadium)^[70] that can operate with mildly acidic electrolytes such as ZnSO₄ in water.^[4] MnO₂ offers operating voltages ≈1.3 and ≈0.9 V higher than those for M_xV_nO_m and organic cathodes, respectively,^[71] thus enabling larger energy densities. CB and a polymeric binder are added to improve the electronic conductivity and structural stability of MnO₂ during cycling. Polyvinylidene fluoride was selected as the binder to circumvent electrode dissolution by water (formulations based on carboxymethyl cellulose were avoided due to its water solubility).

We focused on the α -MnO₂ polymorph given its channel structure providing diffusion pathways for electrolyte ions.^[72] XRD patterns in Figure 7a confirm the presence of α -MnO₂, where the diffraction peaks at $2\theta = 28.8^\circ$, 37.5° , and 60.3° are ascribed

to the (310), (211), and (521) planes, respectively (JCPDS NO. 44-0141).^[73] The cyclic voltammetry curves in Figure S17, Supporting Information show redox peaks for the composite α -MnO₂ cathode with a significant current response (maximum peak current of 6.75 mA·cm⁻²). A reversible Zn²⁺ insertion/extraction in the α -MnO₂ is observed for all the GPEs, where Zn²⁺ extraction occurs in the cathodic zone at 1.70–1.84 V versus Zn/Zn²⁺ (charge) and the Zn²⁺ insertion into the channel structure of α -MnO₂ occurs at 1.20–1.25 versus Zn/Zn²⁺ during discharge.^[71] These curves contrast with the sloping plateaus observed for commercial α -MnO₂, indicating the presence of abundant electrode/electrolyte interfaces and limited ion diffusion path in the synthesized cathode.^[74]

Galvanostatic charge/discharge curves of Zn/ α -MnO₂ full cells at 100 mA·g⁻¹ comprising different GPEs are shown in Figure 7b (1 C \approx 290 mA·g⁻¹).^[4] The cell with a glass microfibre separator soaked with 2 M ZnSO₄·H₂O electrolyte presents an initial sloping plateau at \approx 1.40 V followed by a long and flat discharge plateau at \approx 1.26 V, delivering a first discharge capacity of 219 mAh·g⁻¹. This curve is compatible with the redox reactions originating from the insertion/extraction of Zn²⁺ and H⁺ in MnO₂-based ZIBs.^[72] The discharge capacity is slightly increased to 222 mAh·g⁻¹ when the ChNF-0.8/Glu-0.25 GPE is applied (short-circuit occurs during the first cycle for the ChNF-0.8/Glu-2.0 GPE). However, delivered capacity drops to \approx 155 mAh·g⁻¹ for GPEs containing 1.0 or 1.5 wt% of ChNFs. Gels composed of an excessive amount of ChNFs remain too dense for an efficient diffusion of Zn²⁺ between Zn and α -MnO₂ electrodes. Su et al.^[74] ascribed the first voltage plateau (region I) to the H⁺ insertion, while they stated that the voltage plateau in the second plateau (region II) results from Zn²⁺ insertion. It seems therefore that the presence of ChNFs in the gels facilitates Zn²⁺ insertion compared to the glass fiber separator soaked in 2 M ZnSO₄·H₂O (extending the specific capacity from \approx 110 to \approx 180 mAh·g⁻¹) while hindering H⁺ insertion into the α -MnO₂ cathode.

The operating lifespan with different GPEs was investigated because it is considered a prime requisite toward environmentally and economically sustainable batteries.^[75] A marked capacity fading during cycling at 100 mA·g⁻¹ is observed in Figure 7c when a glass microfibre separator–liquid electrolyte pair is used, delivering 14 mAh·g⁻¹ of capacity after 600 cycles. This decay, characteristic of α -MnO₂ cathodes, may be explained by the formation of passivating by-products at the surfaces of both the anode (ZnO, Zn(OH)₂) and cathode (Mn(OH)₂, MnOOH), together with the dissolution of the active material.^[4] The pronounced initial capacity decay in the presence of ChNF GPEs (low Coulombic efficiencies during the first 10 cycles, Figure S18a, Supporting Information) can be explained by the formation of unstable Mn³⁺ by reduction of Mn⁴⁺, which then reacts to yield soluble Mn²⁺ into the electrolyte.^[76] However, all the ChNF GPEs present a less pronounced decay after the initial 100 cycles in comparison with the glass microfibre separator. In particular, the ChNF-0.8/Glu-0.25 GPE keeps a discharge capacity of 41 mAh·g⁻¹ after 600 cycles, representing a capacity retention of 19% over the 6% observed for the glass microfibre separator. This increased stability upon cycling highlights the suitability of biopolymer electrolytes for sustainable energy storage systems beyond LIBs. Figure S18b,c, Supporting Information summarizes the rate performance of ChNF GPEs and the corresponding Coulombic ef-

iciencies. The delivered capacity decays with the cycling rate for all the samples due to an increased Ohmic polarization and a reduced ability of Zn²⁺ and H⁺ to be inserted in the channels of the α -MnO₂ structure.^[77,78] Generally, the rate capability of ChNF GPEs is comparable to that observed for glass microfibre separators. For example, at current densities above 500 mA·g⁻¹, ChNF-0.8/Glu-0.25 and ChNF-0.8/Glu-1.0 GPEs offer 61 and 57 mAh·g⁻¹, respectively, which is slightly above the 54 mAh·g⁻¹ delivered by the glass microfibre.

To demonstrate the potential of developed GPEs and current collectors for transient energy storage applications, a ZIB consisting of a Zn foil, an α -MnO₂ cathode, a ChNF-0.8/Glu-1.0 GPE and PBAT/CB 20 wt% current collectors was fabricated. As shown in Figure 7d, the whole battery (40 × 60 mm) is encased by a 38 μ m thick PCL film. This encasing protects the battery from the exterior during electrochemical cycling while it enables a quick degradation at temperatures above the melting temperature of PCL (\approx 61 °C). The constructed battery prototype can provide an open-circuit voltage of 1.58 V (Figure S19, Supporting Information), which is sufficient to power low power consumption electronic components and is 0.46 V above our previous transient ZIB prototype.^[79] Furthermore, the transiency of the assembled Zn/ α -MnO₂ system is proven in Figure 7e, where the battery components begin to disintegrate after 2 h immersion in water (pH of 5.9) at 70 °C and almost completely disintegrates after 101 days (Figure S20, Supporting Information). Initially, water-soluble hydrolysis products (caproic acid, succinic acid, valeric acid, and butyric acid) are expelled from the PCL encasing. After 2 h, the water diffuses into the battery components, where PBAT/CB current collectors are slowly hydrolytically degraded into adipic acid, terephthalic acid, and 1,4-butanediol and the CB forms a colloidal solution once the PBAT host is degraded. Besides, the acetal linkages between hydroxyl groups in the ChNF GPE are hydrolyzed to hemiacetals with water as nucleophile and alcohol as leaving groups so that the gel electrolyte is disintegrated. The zinc foil suffers aqueous corrosion and slowly dissolves to provide zinc cations, while the α -MnO₂ cathode undergoes reductive dissolution processes to render Mn²⁺.^[24] Importantly, as no toxic degradation products (polyester degradation products, or dispersed CB and α -MnO₂) result upon degradation, this design improves our previous transient LIB containing the genotoxic V₂O₅.^[23]

4. Conclusions

This work presents the synthesis of a bio-based GPE that balances the frequently mutually exclusive aspects of material renewability, biodegradability, processability, thermo-mechanical performance, operating lifespan, and rate capability. ChNFs are extracted from mushrooms under mild conditions and applied in the energy storage field for the first time. This work also represents the first example of a gel based on ChNFs isolated from fungal resources. The structural flexibility and large aspect ratio of these biocolloids facilitate their physical assembly into hierarchically ordered mesoporous gels which after 2 M ZnSO₄ infiltration offer an excellent Zn²⁺ conductivity of 54.1 mS·cm⁻¹. Besides, ChNF surfaces facilitate ion pair dissociation into Zn²⁺ and SO₄²⁻ to reach a maximum Zn²⁺ transference number of 0.468. The mechanical adaptability of the gels and the strong

water interaction of nanochitin with EU values up to 4046% enable a stable and reversible Zn electrodeposition with low overpotential. Long operating lifespans in symmetric Zn/Zn cells functioning at areal current densities as high as $9.5 \text{ mA}\cdot\text{cm}^{-2}$ are observed due to the homogeneous Zn^{2+} flux through the mesoporous gel that is able to withstand dendrite puncture. When assembled in a Zn/ α -MnO₂ full cell, the ChNF-0.8/Glu-0.25 GPE provides $41 \text{ mAh}\cdot\text{g}^{-1}$ after 600 cycles at $100 \text{ mA}\cdot\text{g}^{-1}$, while the capacity delivered by the glass microfibre separator rapidly decays to $14 \text{ mAh}\cdot\text{g}^{-1}$. After optimization of three polyesters and CB, biodegradable current collectors with electric conductivities reaching $494.8 \text{ S}\cdot\text{m}^{-1}$ and elongation at a break of 877% are fabricated. Importantly, ChNF GPEs and polyester/CB current collectors are applied to develop a prototype of a transient battery that degrades in water at 70 °C. Thereby, this transient ZIB demonstrates the applicability of fungal resources for green and electrochemically competitive secondary batteries not relying on critical raw materials.

Supporting Information

Supporting Information is available from the Wiley Online Library or from the author.

Acknowledgements

The Global Training Program of the Basque Government is acknowledged. The authors are grateful for the financial support from the “2021 Euskampus Missions 1.0. Programme” granted by Euskampus Fundazioa and the University of the Basque Country (Convocatoria de ayudas a grupos de investigación GIU21/010). Technical and human support provided by SGIker (UPV/EHU, MICINN, GV/EJ), EGEF, and ESF) is gratefully acknowledged. The authors also thank ETH Zurich for financial support.

Conflict of Interest

The authors declare no conflict of interest.

Data Availability Statement

The data that support the findings of this study are available in the supplementary material of this article.

Keywords

chitin nanofibrils, gel polymer electrolytes, transient, zinc-ion batteries, zinc plating/stripping

Received: April 22, 2023
Revised: June 23, 2023
Published online: July 11, 2023

- [1] M. Fichtner, K. Edström, E. Ayerbe, M. Berecibar, A. Bhowmik, I. E. Castelli, S. Clark, R. Dominko, M. Erakca, A. A. Franco, A. Grimaud, B. Horstmann, A. Latz, H. Lorrmann, M. Meeus, R. Narayan, F. Pammer, J. Ruhland, H. Stein, T. Vegge, M. Weil, *Adv. Energy Mater.* **2022**, *12*, 2102904.

- [2] G. Harper, R. Sommerville, E. Kendrick, L. Driscoll, P. Slater, R. Stolkin, A. Walton, P. Christensen, O. Heidrich, S. Lambert, A. Abbott, K. Ryder, L. Gaines, P. Anderson, *Nature* **2019**, *575*, 75.
 [3] Y. Liang, H. Dong, D. Aurbach, Y. Yao, *Nat. Energy* **2020**, *5*, 646.
 [4] L. E. Blanc, D. Kundu, L. F. Nazar, *Joule* **2020**, *4*, 771.
 [5] D. Zhou, D. Shanmukaraj, A. Tkacheva, M. Armand, G. Wang, *Chem* **2019**, *5*, 2326.
 [6] L. Lv, B. Hui, X. Zhang, Y. Zou, D. Yang, *Chem. Eng. J.* **2023**, *452*, 139443.
 [7] S. Ferrari, M. Falco, A. B. Muñoz-García, M. Bonomo, S. Brutti, M. Pavone, C. Gerbaldi, *Adv. Energy Mater.* **2021**, *11*, 2100785.
 [8] N. Mittal, S. Tien, E. Lizundia, M. Niederberger, *Small* **2022**, *18*, 2107183.
 [9] F. Santos, A. Urbina, J. Abad, R. López, C. Toledo, A. J. Fernández Romero, *Chemosphere* **2020**, *250*, 126273.
 [10] M. Iturrondobeitia, O. Akizu-Gardoki, O. Amondarain, R. Minguez, E. Lizundia, *Adv. Sustainable Syst.* **2021**, *6*, 2100308.
 [11] European Association for Storage of Energy, <https://ease-storage.eu/wpcontent/uploads/2022/06/Energy-Storage-Targets-2030-and-2050-Full-Report.pdf>, (accessed: June 2023).
 [12] C. Clarke, I. D. Williams, D. A. Turner, *Resour., Conserv. Recycl.* **2019**, *141*, 465.
 [13] A. S. Brandão, A. Gonçalves, J. M. R. C. A. Santos, *J. Cleaner Prod.* **2021**, *295*, 126407.
 [14] C. Xu, M. Nasrollahzadeh, M. Selva, Z. Issaabadi, R. Luque, *Chem. Soc. Rev.* **2019**, *48*, 4791.
 [15] W. M. F. B. W. Nawawi, M. Jones, R. J. Murphy, K.-Y. Lee, E. Kontturi, A. Bismarck, *Biomacromolecules* **2020**, *21*, 30.
 [16] N. A. R. Gow, J. P. Latge, C. A. Munro, *Microbiol. Spectrum* **2017**, *5*, 3.
 [17] W. M. Fazli Wan Nawawi, K.-Y. Lee, E. Kontturi, R. J. Murphy, A. Bismarck, *ACS Sustainable Chem. Eng.* **2019**, *7*, 6492.
 [18] M. Berroci, C. Vallejo, E. Lizundia, *ACS Sustainable Chem. Eng.* **2022**, *10*, 14280.
 [19] L. Mendoza, W. Batchelor, R. F. Tabor, G. Garnier, *J. Colloid Interface Sci.* **2018**, *509*, 39.
 [20] N. Mittal, A. Ojanguren, N. Cavin, E. Lizundia, M. Niederberger, *Adv. Funct. Mater.* **2021**, *31*, 2101827.
 [21] N. Mittal, A. Ojanguren, M. Niederberger, E. Lizundia, *Adv. Sci.* **2021**, *8*, 2004814.
 [22] M.-M. Titirici, *Adv. Energy Mater.* **2021**, *11*, 2003700.
 [23] X. Aebly, A. Poulin, G. Siqueira, M. K. Hausmann, G. Nyström, *Adv. Mater.* **2021**, *33*, 2101328.
 [24] L. A. Wehner, N. Mittal, T. Liu, M. Niederberger, *ACS Cent. Sci.* **2021**, *7*, 231.
 [25] M. H. Alfaruqi, S. Islam, J. Gim, J. Song, S. Kim, D. T. Pham, J. Jo, Z. Xiu, V. Mathew, J. Kim, *Chem. Phys. Lett.* **2016**, *650*, 64.
 [26] N. E. Mushi, N. Butchosa, Q. Zhou, L. A. Berglund, *J. Appl. Polym. Sci.* **2014**, *131*, 40121.
 [27] D. Raabe, P. Romano, C. Sachs, H. Fabritius, A. Al-Sawalmih, S.-B. Yi, G. Servos, H. G. Hartwig, *Mater. Sci. Eng., A* **2006**, *421*, 143.
 [28] M. Jones, M. Kujundzic, S. John, A. Bismarck, *Mar. Drugs* **2020**, *18*, 64.
 [29] M. Kaya, M. Mujtaba, H. Ehrlich, A. M. Salaberria, T. Baran, C. T. Amemiya, R. Galli, L. Akyuz, I. Sargin, J. Labidi, *Carbohydr. Polym.* **2017**, *176*, 177.
 [30] Y. Wang, Y. Chang, L. Yu, C. Zhang, X. Xu, Y. Xue, Z. Li, C. Xue, *Carbohydr. Polym.* **2013**, *92*, 90.
 [31] P. Sikorski, R. Hori, M. Wada, *Biomacromolecules* **2009**, *10*, 1100.
 [32] N. Yousefi, M. Jones, A. Bismarck, A. Mautner, *Carbohydr. Polym.* **2021**, *253*, 117273.
 [33] Y. Lu, L. Weng, L. Zhang, *Biomacromolecules* **2004**, *5*, 1046.
 [34] W. M. F. W. Nawawi, K.-Y. Lee, E. Kontturi, A. Bismarck, A. Mautner, *Int. J. Biol. Macromol.* **2020**, *148*, 677.
 [35] L. Bai, L. Liu, M. Esquivel, B. L. Tardy, S. Huan, X. Niu, S. Liu, G. Yang, Y. Fan, O. J. Rojas, *Chem. Rev.* **2022**, *122*, 11604.

- [36] E. Lizundia, T.-D. Nguyen, R. J. Winnick, M. J. MacLachlan, *J. Mater. Chem. C* **2021**, 9, 796.
- [37] N. Quennouz, S. M. Hashmi, H. S. Choi, J. W. Kim, C. O. Osuji, *Soft Matter* **2016**, 12, 157.
- [38] V. Calabrese, J. C. Muñoz-García, J. Schmitt, M. A. da Silva, J. L. Scott, J. Angulo, Y. Z. Khimyak, K. J. Edler, *J. Colloid Interface Sci.* **2019**, 535, 205.
- [39] E. Lizundia, D. Kundu, *Adv. Funct. Mater.* **2021**, 31, 2005646.
- [40] F. Zeng, Y. Sun, B. Hui, Y. Xia, Y. Zou, X. Zhang, D. Yang, *ACS Appl. Mater. Interfaces* **2020**, 12, 43805.
- [41] I. Dueramae, M. Okhawilai, P. Kasemsiri, H. Uyama, *Sci. Rep.* **2021**, 11, 13268.
- [42] W. Qiu, Y. Li, A. You, Z. Zhang, G. Li, X. Lu, Y. Tong, *J. Mater. Chem. A* **2017**, 5, 14838.
- [43] A. M. Hyde, S. L. Zultanski, J. H. Waldman, Y.-L. Zhong, M. Shevlin, F. Peng, *Org. Process Res. Dev.* **2017**, 21, 1355.
- [44] Z. Zhang, Y. Liu, S. Lin, Q. Wang, *J. Polym. Res.* **2020**, 27, 228.
- [45] R. Rudra, V. Kumar, P. P. Kundu, *RSC Adv.* **2015**, 5, 83436.
- [46] R. D. McKerracher, J. Guzman-Guemez, R. G. A. Wills, S. M. Sharkh, D. Kramer, *Adv. Energy Sustainability Res.* **2021**, 2, 2000059.
- [47] W. Liu, D. Lin, A. Pei, Y. Cui, *J. Am. Chem. Soc.* **2016**, 138, 15443.
- [48] B. Wicklein, A. Kocjan, G. Salazar-Alvarez, F. Carosio, G. Camino, M. Antonietti, L. Bergström, *Nat. Nanotechnol.* **2014**, 10, 277.
- [49] C. M. Walters, G. K. Matharu, W. Y. Hamad, E. Lizundia, M. J. MacLachlan, *Chem. Mater.* **2021**, 33, 5197.
- [50] R. Bai, J. Yang, Z. Suo, *Eur. J. Mech., A: Solids* **2019**, 74, 337.
- [51] A. Ojanguren, N. Mittal, E. Lizundia, M. Niederberger, *ACS Appl. Mater. Interfaces* **2021**, 13, 21250.
- [52] Y. Ma, X. Xie, R. Lv, B. Na, J. Ouyang, H. Liu, *ACS Sustainable Chem. Eng.* **2018**, 6, 8697.
- [53] X. Jia, Y. Yang, C. Wang, C. Zhao, R. Vijayaraghavan, D. R. MacFarlane, M. Forsyth, G. G. Wallace, *ACS Appl. Mater. Interfaces* **2014**, 6, 21110.
- [54] T. Yan, Y. Zou, X. Zhang, D. Li, X. Guo, D. Yang, *ACS Appl. Mater. Interfaces* **2021**, 13, 9856.
- [55] X. Li, H. Yao, Y. Li, D. Yuan, Y. Chen, M. W. Wong, Y. Zhang, H. Zhang, *J. Mater. Chem. A* **2023**.
- [56] C. Zhao, J. Niu, C. Xiao, Z. Qin, X. Jin, W. Wang, Z. Zhu, *Chem. Eng. J.* **2022**, 444, 136537.
- [57] Y. Hao, D. Feng, L. Hou, T. Li, Y. Jiao, P. Wu, *Adv. Sci.* **2022**, 9, 2104832.
- [58] X. Zhang, J.-P. Hu, N. Fu, W.-B. Zhou, B. Liu, Q. Deng, X.-W. Wu, *InfoMat* **2022**, 4, e12306.
- [59] A. Yurtsever, P.-X. Wang, F. Priante, Y. M. Jaques, K. Miyata, M. J. MacLachlan, A. S. Foster, T. Fukuma, *Small Methods* **2022**, 6, 2200320.
- [60] H. Yang, Z. Chang, Y. Qiao, H. Deng, X. Mu, P. He, H. Zhou, *Angew. Chem., Int. Ed.* **2020**, 59, 9377.
- [61] C. Ma, W. Cui, X. Liu, Y. Ding, Y. Wang, *InfoMat* **2022**, 4, e12232.
- [62] Y. Zhu, Y. Cui, H. N. Alshareef, *Nano Lett.* **2021**, 21, 1446.
- [63] R. Wang, W. Li, L. Liu, Y. Qian, F. Liu, M. Chen, Y. Guo, L. Liu, *J. Electroanal. Chem.* **2019**, 833, 63.
- [64] W. Bauhofer, J. Z. Kovacs, *Compos. Sci. Technol.* **2009**, 69, 1486.
- [65] P. Tan Thong, T. Sadhasivam, N.-I. Kim, Y. A. Kim, S.-H. Roh, H.-Y. Jung, *Energy* **2021**, 221, 119856.
- [66] P. Zhu, D. Gastol, J. Marshall, R. Sommerville, V. Goodship, E. Kendrick, *J. Power Sources* **2021**, 485, 229321.
- [67] X. Meng, V. Bocharova, H. Tekinalp, S. Cheng, A. Kisliuk, A. P. Sokolov, V. Kunc, W. H. Peter, S. Ozcan, *Mater. Des.* **2018**, 139, 188.
- [68] C. S. M. Pereira, V. M. T. M. Silva, A. E. Rodrigues, *Green Chem.* **2011**, 13, 2658.
- [69] P. Majgaonkar, R. Hanich, F. Malz, R. Brüll, *Chem. Eng. J.* **2021**, 423, 129952.
- [70] A. Kulkarni, G. S. Kumar, J. Kaur, K. Tikoo, *Inhalation Toxicol.* **2014**, 26, 772.
- [71] L. Wang, J. Zheng, *Mater. Today Adv.* **2020**, 7, 100078.
- [72] Y. Liao, H.-C. Chen, C. Yang, R. Liu, Z. Peng, H. Cao, K. Wang, *Energy Storage Mater.* **2022**, 44, 508.
- [73] J. Yang, S. Ren, B. Su, Y. Zhou, G. Hu, L. Jiang, J. Cao, W. Liu, L. Yao, M. Kong, J. Yang, Q. Liu, *Catal. Lett.* **2021**, 151, 2964.
- [74] W. Sun, F. Wang, S. Hou, C. Yang, X. Fan, Z. Ma, T. Gao, F. Han, R. Hu, M. Zhu, C. Wang, *J. Am. Chem. Soc.* **2017**, 139, 9775.
- [75] J. Porzio, C. D. Scown, *Adv. Energy Mater.* **2021**, 11, 2100771.
- [76] T. Zhang, Y. Tang, S. Guo, X. Cao, A. Pan, G. Fang, J. Zhou, S. Liang, *Energy Environ. Sci.* **2020**, 13, 4625.
- [77] M. Winter, R. J. Brodd, *Chem. Rev.* **2004**, 104, 4245.
- [78] V. J. Ovejas, A. Cuadras, *J. Power Sources* **2019**, 418, 176.
- [79] N. Mittal, A. Ojanguren, D. Kundu, E. Lizundia, M. Niederberger, *Small* **2023**, 19, 2206249.